Materials Today Communications 45 (2025) 112276

Contents lists available at ScienceDirect

Materials Today Communications

journal homepage: www.elsevier.com/locate/mtcomm

Non-equilibrium molecular dynamics simulation of anisotropic heat transfer and thermal conductivity of single crystalline magnesium antimonide

Seçkin D. Günay [a], Ünsal Akdere [a], Çetin Taşseven [a,b,*]

[a] Department of Physics, Faculty of Science and Letter, Yıldız Technical University, Davutpaşa Campus, Istanbul 34210, Turkey
[b] Physics, Faculty of Science, University of East Anglia, Norwich Research Park, Norwich NR4 7TJ, United Kingdom

ARTICLE INFO

Keywords:
Magnesium antimonide
Non-equilibrium molecular dynamics
Thermal conductivity

ABSTRACT

Magnesium antimonide (Mg_3Sb_2) based materials are potential candidates as thermoelectric materials in thermoelectric devices with enhanced performance. Thermal conductivity and its temperature dependence are key factors in their practical applications. The present work aims to evaluate the temperature dependence of lattice thermal conductivity (κ_L) of single crystalline Mg_3Sb_2 along the in-plane and out-of-plane directions between 300K and 700K. Non-equilibrium molecular dynamics (NEMD) simulation combined with two regions thermostatting method is followed to mimic the real experiment. It is found that the κ_L exhibits strong anisotropy at low and mid temperatures and becomes nearly isotropic at high temperatures. The κ_L is significantly low along both in-plane and out-of-plane directions, and reduces from $\sim$ 2.1 to $\sim$ 1.1 W $m^{-1}K^{-1}$and $\sim$ 1.3 to $\sim$ 1.1 W $m^{-1}K^{-1}$, respectively, but with different temperature dependences. Deviating from the typical T^{-1} law, calculated κ_L demonstrates an anomalously weaker temperature dependence in the in-plane direction described as $T^{-0.67}$, and even weaker in the out-of-plane direction as $T^{-0.14}$. Anisotropic low thermal conductivity is crucial for searching thermoelectric materials with enhanced figure of merit, and hence this work may provide guideline and encourage future studies on Mg_3Sb_2 based materials.

1. Introduction

Research interest on thermophysical properties of materials is increasing everyday due to high demand for sustainable energy. Thermal conductivity is one of the key properties as a selection criterion for the search of advanced materials as both thermal insulator and conductor in technical applications. High thermal conductivity materials are needed for the development of optoelectronic devices and integrated electronic circuitry for the efficient thermal absorption and dissipation. On the other hand, low thermal conductivity property is also crucial to maintain large temperature difference for efficient thermal insulation and energy harvesting in various applications of thermoelectric materials [1–4]. Thermoelectric materials are critical for advanced energy applications, enabling direct conversion between waste heat and electrical energy. These materials can also generate controlled temperature gradients from applied voltages, making them ideal for efficient heating and cooling systems. Unlike conventional refrigeration or power generation technologies, thermoelectric devices operate silently and without mechanical wear, as they lack moving parts and do not require refrigerants (e.g., ammonia or hydrofluorocarbons) [5,6]. Zintl phases are one of the extensively studied class of efficient thermoelectric materials that are semiconductors with complex structures and a mix of ionic and covalent bonding [7]. Magnesium based thermoelectric materials have attracted great attention in development of high-performance devices for both power generation and solid-state cooling in addition to Mg-ion and Mg-air batteries applications [8,9]. Among them, magnesium antimonide (Mg_3Sb_2) based thermoelectric materials is a promising potential candidate in challenges of searching materials with enhanced thermoelectric performance due to their excellent thermoelectric properties and abundance, non-toxicity, and low cost [9–12]. The efficiency of a thermoelectric material can be measured by the dimensionless thermoelectric figure of merit which is proportional to Seebeck coefficient, electric conductivity, and temperature and inversely proportional to thermal conductivity. Inherently, Mg_3Sb_2 exhibit p-type transport characteristics at room temperature due to the presence of intrinsic Mg vacancies. But it can be obtained in the

* Corresponding author at: Department of Physics, Faculty of Science and Letter, Yıldız Technical University, Davutpaşa Campus, Istanbul 34210, Turkey.
E-mail address: tasseven@yildiz.edu.tr (Ç. Taşseven).

https://doi.org/10.1016/j.mtcomm.2025.112276
Received 12 February 2025; Received in revised form 9 March 2025; Accepted 16 March 2025
Available online 19 March 2025
2352-4928/© 2025 Elsevier Ltd. All rights are reserved, including those for text and data mining, AI training, and similar technologies.

form of p-type or n-type thermoelectric material with enhanced properties by introduction of various dopant. Besides alloying, it has been shown that element substitution and tuning carrier concentration are very effective techniques to enhance the energy conversion efficiency by maximising the figure of merit which is generally found to be higher for n-type Mg_3Sb_2-based materials due to larger bandgap degeneracy and higher carrier mobility than p-type [8,9,13]. The lattice thermal conductivity of single- and poly-crystalline and n-type Mg_3Sb_2 has been reported to be below $\kappa_L = 2.0$ W m^{-1}K^{-1} at low- and mid-temperature with anisotropy in thermal transport properties, *namely* different for in-plane and out-of-plane directions, which renders it more preferable than its analogous commercial materials [9,13–15]. Single crystals of the $Mg_3(Bi,Sb)_2$ alloy exhibit higher charge carrier mobility and lower lattice thermal conductivity compared to polycrystalline samples, as observed in angle-resolved photoemission spectroscopy (ARPES) experiments. These findings highlight the detrimental impact of grain boundaries on thermoelectric performance [16]. Furthermore, the weak temperature dependence of the lattice thermal conductivity in single-crystal Mg_3Sb_2 has been attributed to phonon renormalization effects caused by the strong temperature sensitivity of its interatomic force constants [17]. The intrinsic low thermal conductivity of p-type single crystal Mg_3Sb_2 is arises from large Grüneisen parameters and strong anharmonicity. The presence of grain boundary doesn't significantly affect the lattice thermal conductivity of polycrystalline [15]. The lattice thermal conductivity of Mg_3Sb_2 was suggested to be nearly isotropic with its ratio in-plane and out-of-plane directions (κ_a/κ_c or κ_c/κ_a) between ≈ 1.05 and ≈ 1.10 [18–20]. However later, it was argued that there is anisotropy with the ratio of $\kappa_a/\kappa_c \approx 1.22$ [17] and $\kappa_a/\kappa_c \approx 1.44$ [21], due to the difference in average group velocities and chemical bonding along intralayer and interlayer directions. Despite the fact that significant work has been carried out, the anisotropy of the lattice thermal conductivity in the single crystal Mg_3Sb_2 still seems like an issue that needs to be worked on as it is one of the key merits for the development of thermoelectric devices. Thereby, in this paper we aimed to investigate the lattice thermal conductivity in the single crystal Mg_3Sb_2 using the method of non-equilibrium molecular dynamics (NEMD) simulation which mimics real experiment and has been ignored so far in previous studies. The method is based on time reversible equations of motion and introduces the novel concept of substituting external thermodynamic conditions with internal control variables to maintain non-equilibrium states.

2. Methodology

2.1. Crystal structure

The crystal structure of Mg_3Sb_2 adapted from the Materials Project (mp-2646) from database version v2023.11.1. [22] is shown in Fig. 1. The Mg3Sb2 is described as the Zintl-type structure and crystallizes in the trigonal P^{-}3m1 space group with five atoms per primitive cell. There are two distinct Mg^{+2} sites, labelled as Mg(I) and Mg(II). Mg(I) is at the octahedral site surrounded by six equivalent Sb^{3-} atoms with Mg-Sb bond length 3.11 Å to form $MgSb_6$ octahedra. In the Mg(II) site, Mg^{2+} is bonded to four equivalent Sb^{3-} atoms of Mg-Sb bond lengths 2.82 Å and one longer 2.94 Å to form $MgSb_4$ tetrahedra. Based on its layered Zintl phase structural characteristics Mg_3Sb_2 is also categorized as CaAl2Si2-type compound and written as $MgMg_2Sb_2$ with distinct covalent $[Mg_2Sb_2]^{2-}$ (Mg(II)) layers and ionic Mg^{2-} (Mg(I)) layers [23,24].

2.2. Potential model

There is various type of classical pairwise model potential that could be used to model the inter-ionic interactions for such systems. In this study, MD simulation calculations have been carried using the Buckingham type of rigid ion potential of the form $\phi_{ij}(r) = Z_iZ_j/r + A_{ij}\exp(-r/\rho_{ij}) - C_{ij}/r^6$. Where the first term is the long-range Coulomb interaction, and the second and third terms simply describe the short-range repulsive and attractive van der Walls interactions, respectively. The potential parameters have been previously optimised for the experimental lattice constants $a = b = 4.57$ Å and $c = 7.23$ Å, and first-principles bulk modulus $K = 48.8$ GPa to investigate static structure and ionic transport in molten Mg_3Sb_2 using the hypernetted-chain theory of liquids (HNC) and the molecular dynamics simulation methods [25]. The parameters of the potential are as follows; the effective changes are $Z_{Mg} = 1.32e$ and $Z_{Sb} = -1.98e$, the strength A_{ij} and the hardness ρ_{ij} parameters of short range interactions of ions are $A_{Mg-Sb} = 1.30 \times 10^3$eV, $A_{Mg-Mg} = 9.55 \times 10^3$eV $A_{Sb-Sb} = 9.05 \times 10^3$eV, $\rho_{Mg-Sb} = 0.38$ Å, $\rho_{Mg-Mg} = 0.22$ Å and $\rho_{Sb-Sb} = 0.39$ Å, and van der Waals parameters are $C_{Mg-Sb} = 94.0$ eVÅ^6, $C_{Mg-Mg} = 0.0eV$ Å^6 and $C_{Sb-Sb} = 1.66 \times 10^3$eVÅ^6.

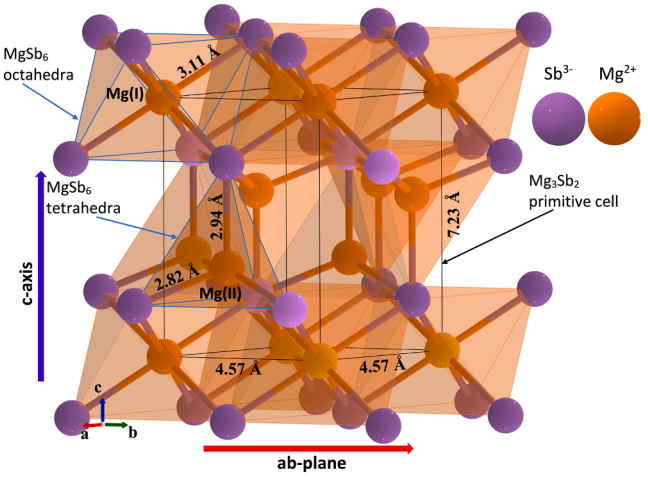


Fig. 1. Crystal structure of Mg_3Sb_2 with space group P^{-}3m1 and illustration of primitive cell, octahedral Mg(I) A-site and tetrahedral Mg(II) site adapted from the Materials Project (mp-2646) from database version v2023.11.1 [22].

Selection of a proper interatomic potential to simulate thermophysical properties of materials like magnesium antimonide is one of the important keys. Semi-empirical pair potentials offer computational efficiency but sacrifice accuracy in capturing the complex physics of thermal transport. Semi-empirical pair potentials are computationally efficient for large-scale systems and long simulations. They are easy to implement, useful for identifying qualitative trends in materials, and perform well in scenarios where electronic effects are minimal, such as high-temperature insulators or semiconductors. However, they come with some limitations, such as the absence of many-body interactions, inaccurate phonon dispersion, and neglect of quantum effects (e.g., incorrect representation of phonon populations at low temperatures). These drawbacks can lead to unstable atomic dynamics in nanostructures, where many-body potentials or machine-learned interatomic potentials may be more suitable. Therefore, it is essential to validate semi-empirical pair potentials carefully against experimental data or ab initio calculations. The potential model that we used here, previously optimised by fitting the parameter to the experimental and the first-principles lattice constants and bulk modulus, used to calculate high temperature structural and ionic transport properties [25] which verifies the correctness of the model potential and parameters within its limitations.

2.3. Computer simulation

2.3.1. Thermal conductivity

The molecular dynamics simulation (MD) is a promising method and

plays important role to study heat transfer and thermal conductivity in bulk materials. There are two popular techniques commonly used for this purpose: Equilibrium molecular dynamics (EMD) and non-equilibrium molecular dynamics (NEMD). EMD relies on the evaluation of heat current fluctuations in a bulk system equilibrated at a specific temperature. Then, the thermal conductivity, which is related to the integration of the heat current autocorrelation function, is calculated using Green-Kubo or Einstein fluctuation relation [26,27]. The NEMD utilizes time reversible equations of motion and introduces the novel concept of substituting external thermodynamic conditions with internal control variables to maintain non-equilibrium states [28]. In comparison to EMD, NEMD mimics real experiment to calculate thermal conductivity by setting up two heat reservoirs kept at different temperatures at the two ends of system, or one in the middle and one at the end of a periodic box, so the heat flux can be calculated directly. Another approach, instead of using thermostats, is to constantly swap the kinetic energy, thus add or remove fixed amount of energy, to impose heat flux directly between two regions in the system [29,30].

In this paper, we follow the methodology of NEMD to study the spatially anisotropic lattice thermal conductivity of single crystal magnesium antimonide in the directions of x and z. Thermal conductivity tensor refers to materials intrinsic tendency to transfer or conduct heat in a diffusive manner. It is a key property that characterises the thermal transport behaviour and determines the operating temperature range of materials. Macroscopically, the conduction of heat is governed by Fourier's Law of heat conduction and the heat conservation law and is expressed as $\vec{J} = -\kappa\vec{\nabla}T$, where $\vec{J}$ is the heat flux, the thermal conductivity κ is a second-rank tensor, and $\vec{\nabla}T$ is the temperature gradient. To calculate κ in NEMD: the temperature gradient can be approximated as $\frac{\partial T}{\partial x_i} = \frac{T_{Hot} - T_{Cold}}{l_{x_i}}$ and the heat flux J_{x_i} is directly measured as the energy $\Delta E_{x_j x_k}$ being transferred between the hot region at T_{Hot} and cold region at T_{Cold} across the plane of cross-sectional area (transverse to the conduction direction) $A = l_{x_j} l_{x_k}$ in the unthermostatted region of length l_{x_i} per simulation time Δt, is which expressed as $J_{x_i} = \frac{\Delta E_{x_j x_k}}{2 l_{x_j} l_{x_k} \Delta t}$, where $x_{i,j,k}$ stands for crystallographic directions x, y, and z.

2.3.2. NEMD methodology

The Large-scale Atomic/Molecular Massively Parallel Simulator (LAMMPS) open-source software used to perform NEMD simulations throughout this study [31]. There are three different NEMD approach implemented in LAMMPS to calculate thermal conductivity: direct Langevin thermostatting (LT) method, heat change method, and Muller-Plathe reverse perturbation or reverse NEMD method [29,30,32]. In this study, we used the Langevin thermostatting method to calculate κ from the temperature profile output, which keeps track of the continuous flow of energy between the hot and cold Langevin thermostats.

There exist four essential stages of NEMD in this work to perform heat transport simulation at a specific temperature represented with a flowchart in Fig. 2. Following the definition of interatomic potential, in Stage 1 the energy of the simulation box of supercell constructed by replicating the unit cell $a \times b \times c$ of Mg_3Sb_2 as $80a \times 20b \times 20c$ and $20a \times 20b \times 80c$ are minimized by iteratively adjusting coordinates of particles in order to calculate thermal conductivity in two different crystallographic directions x and z, respectively. Then, stress and temperature relaxation simulation are carried out with the isothermal-isobaric (NPT) equilibration step to relax the simulation box with periodic boundary conditions in all directions, and update the positions and velocities of atoms at the desired temperatures between $T = 300$ K -700 K and pressure $P = 1$ atm. This will allow the box size and shape to vary, namely the simulation box shrinks or expands until the optimum configuration is approximated. To obtain the equilibrated simulation box, each simulation was independently started at 300 K and gradually heated to the desired temperature $T = 300, 350, \ldots, 700$ K. The equilibration simulation time was increased accordingly from

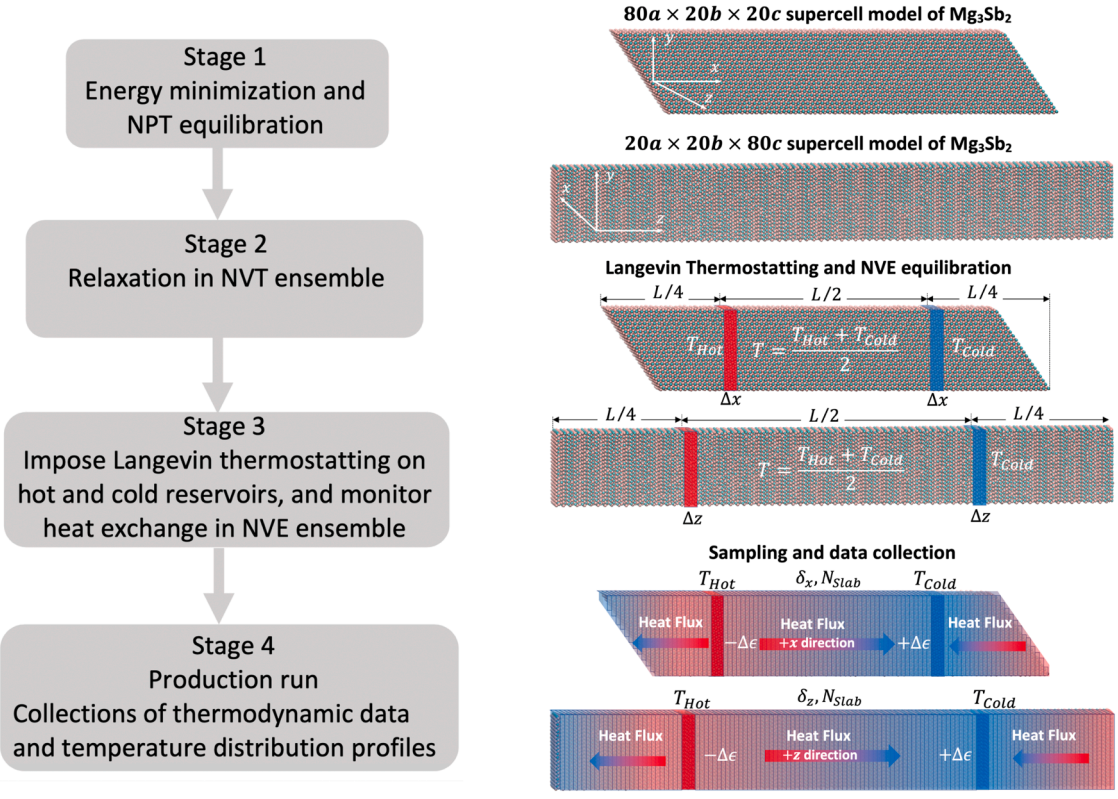


Fig. 2. Flowchart of the stages and schematic representation of the three-dimensional periodic simulation cell of non-equilibrium molecular dynamics simulation using two region Langevin thermostatting method for heat transport in-plane (x-direction) and out-of-plane (z-direction).

200 ps to 700 ps as the temperature increases, in order to prevent instabilities due to rapid increase of energy. In second stage, a relaxation run for the whole system in the isothermal-isochoric NVT (canonical) ensemble is further conducted at the temperature T for 200 ps to enhance the equilibrium. Stage 3 is the starting stage of the LT method where the temperature and position of the hot and cold regions are defined and equilibrated for 200 ps to obtain the steady state. During this process, the temperature of two regions is controlled separately by means of Langevin thermostat while the remaining of the system evolved freely in microcanonical NVE (constant energy and volume) ensemble, and the amount of heat added or removed by the regions is tracked. The temperature of the two reservoirs, which are centred at $x_{Hot} = L_{x_i}/4$ and $x_{Cold} = 3L_{x_i}/4$ with fixed width of Δx_i, are defined as $T_{Hot} = T + \Delta T$ and $T_{Cold} = T - \Delta T$. The final stage (stage 4) of the LT of NEMD simulation is the production stage and corresponds to sampling and collecting data. This was executed for $1ns$. Temperature profile of the system in the direction of heat flux is calculated based on the translational kinetic energy per particle. The whole simulation box is divided into $N_{slab} = 100$ slabs of thickness $\delta_{x_i} = L_{x_i}/N_{slab}$, which varies depending on temperature, in the direction of heat flux. Also note that, the temperature of the hot and cold regions is still controlled by the Langevin thermostats. While periodic boundary conditions are applied in the heat flux directions, free boundary conditions are applied in the other directions.

3. Results and discussion

In this section we present the simulation results and discussion of spatially anisotropic lattice temperature profiles, heat flux evaluations and thermal conductivities of single crystals Mg_3Sb_2 based on NEMD simulations combined with two region LT method. The supercells with dimensions of $80a \times 20b \times 20c$ and $20a \times 20b \times 80c$ consist of hot and cold thermostats and heat flux region which is divided into $N_{slab} = 100$ slices along the corresponding crystallographic directions x (in-plane) and z (out-of-plane). Each slab contains 960 Mg atoms and 640 Sb atoms, and have the thickness of $\delta_{x,z} = L_{x,z}/N$, where $N = 16 \times 10^4$ is the total number of atom in the supercell. Calculations were carried out for the temperature range of $T = 300$ K -700 K at 50 K intervals with the temperature of hot thermostat $T_{Hot} = T + 10$ K and cold thermostat $T_{cold} = T - 10$ K of sizes $\Delta x \times 20b \times 20c$ and $20a \times 20b \times \Delta z$ in the heat flow directions x and z, respectively. Fig. 3 displays the temperature profiles in single crystals Mg_3Sb_2 in the heat flow directions x and z at five temperatures ($T = 300,\ 400,\ \ldots,\ 700$ K) only for a better view. The hot and cold regions with fixed width of $\Delta x = \Delta z = 20\mathring{A}$ are located at $L_{x,z}/4$ and $3L_{x,z}/4$, respectively, for both in-plane and out-of-plane directions. Note that, due to the periodic boundary conditions in the heat flux directions the separation between the hot and cold the regions should be $L_{x,z}/2$ but can be located at any positions. The temperature at the $N_{slab} = 100$ slabs generated by the average temperature of all atoms in each slab using the relation $\frac{3}{2}Nk_BT = \frac{1}{2}\sum_{i=1}^{N} m_i v_i^2$. The temperature gradient between the reservoirs displays a linear trend which indicates the uniform heat transfer. Near the hot and cold reservoirs temperature has nonlinear behaviour due to rapid energy exchange between the kinetic and potential energy. Therefore, these regions were not taken into account for the linear fitting to obtain the temperature gradient ∇T. Two separate regions between the positions $-L_{x,z}/4$ and $L_{x,z}/4$, and $L_{x,z}/4$ and $3L_{x,z}/4$ is considered for the fitting. The temperature gradient was then determined as the average of the absolute values of the slopes in these regions.

In Fig. 4-a the time dependent heat flow in-plane and out-of-plane

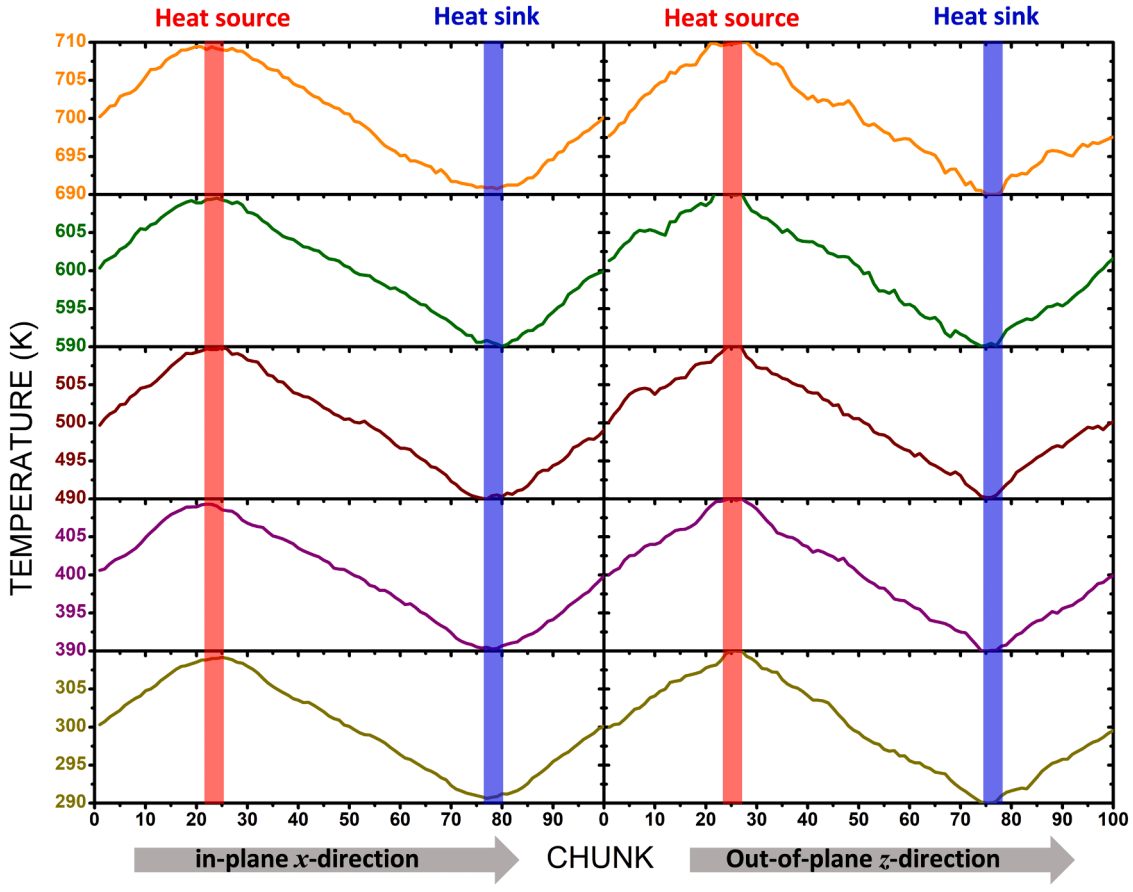


Fig. 3. Temperature profiles in single crystals Mg_3Sb_2 in the heat flow directions x (in-plane) and z (out-of-plane) at the temperatures of $T = 300$ K, 400 K, 500 K, 600 K, and 700 K.

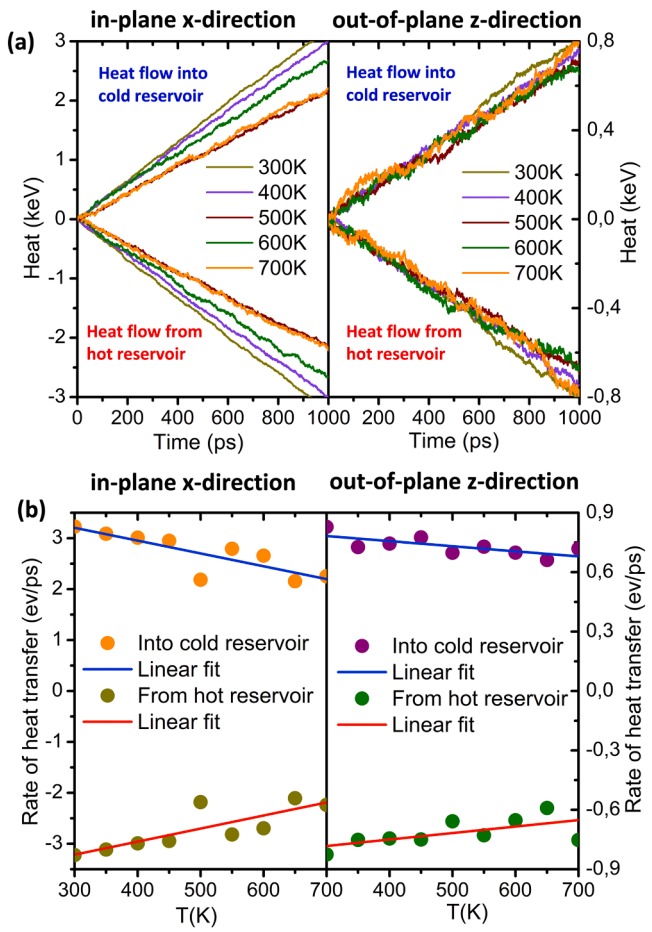


Fig. 4. a) Time dependency of heat flow from the hot region into the cold region in single crystals Mg_3Sb_2 in the directions of x (in-plane) and z (out-of-plane) at $T = 300,\ 400,\ 500,\ 600$ and $700K$ b) The rate of heat transfer versus temperature $(dE_{x_i}/dt)_T$ obtained from the slop of heat flow at constant temperature T.

directions from the hot region into the cold region is compared at the temperatures of $T = 300\ ,\ 400\ ,\ \ldots,\ 700$ K. As expected, the energy of the hot and cold regions exhibits an increasing and decreasing linear variation over the simulation time. The conservation of energy in the model supercells is verified by the approximately equal amount of absolute energy of the reservoirs. The heat flux in-plane and out-of-plane was calculated from $J_{xi} = (dE_{xi}/dt)_T/A$. The rate of heat transfer $(dE_{xi}/dt)_T$ from hot reservoir and into cold is presented in Fig. 4-b which further confirms that the total energy remains constant. The equation absolute rate of heat transfer as a function of temperature was obtained from the calculated average of fitted coefficients for hot and cold reservoirs: $(dE_x/dt)_T = \pm 3.97 \mp 2.54 \times 10^{-3} T(\mathrm{eVps}^{-1})$ in-plane x-direction and $(dE_z/dt)_T = \pm 0.87 \mp 2.93 \times 10^{-4} T(\mathrm{eVps}^{-1})$ out-of-plane z-direction. This result exhibits that the heat transfer along the in-plane direction is about one order of magnitude faster than that of out-of-plane direction in single crystal Mg_3Sb_2 which suggests that Mg_3Sb_2 is a potential thermoelectric material with anisotropic heat transfer property.

The system size in non-equilibrium molecular dynamics (NEMD) simulations using the two-region Langevin thermostat method can significantly influences the observed thermal conductivity anisotropy in a single crystallite. If the size of the simulation along the heat flux direction is not large enough, the hot and cold thermostats may occupy a larger fraction of the simulation box, creating overlapping temperature gradients which distorts the linear response regime. The unit cell was replicated 80 times of size along the desired heat flux directions in order to ensure a well-defined transport central region with minimal thermostat interference. The temperature profile (Fig. 3) with a linear central transport region and the heat flow (Fig. 4-a) indicate that the size is sufficiently large to along both in-plane and out-of-plane directions, and the present NEMD simulations reliable predict the anisotropy in thermal conductivity within the limits of the interatomic potential model used here. Also note that, the spectral transmission function T(ω) would be useful which describes how vibrational energy at frequency ω is transmitted through the system. It acts like a filter that determines which phonon frequencies contribute to heat flow. However, inherent anharmonicity in NEMD simulation and artificial damping in Langevin thermostats makes it challenging to extract harmonic T(ω) directly from heat flux

The lattice thermal conductivity κ_L is the dominant component of total thermal conductivity $\kappa = \kappa_L + \kappa_e$ as the electronic part κ_e does not have significant contribution in most layered crystals due to their semiconducting of isolating nature. Mg_3Sb_2 is a semiconductor material with high Seebeck coefficient and large electronic band gap [8,9,13]. This limits the free charge carrier population, enhances electrical resistivity and reduces the electronic thermal conductivity via the Wiedemann-Franz law $\kappa_e = L\sigma T$, where L is the Lorentz number, and σ is electronic conductivity. Most crystalline solids display T^{-1} type of temperature-dependent κ_L. Moreover, it has been suggested that grain boundary scattering due to the grain boundary segregation has minor effect on the thermal conductivity of Mg_3Sb_2 since a rather small difference was observed between κ_L of polycrystalline and single crystalline Mg_3Sb_2 [15,19] Fig. 5 shows the temperature dependence of lattice thermal conductivity κ_L of single crystal Mg_3Sb_2 between 300 K and 700 K. The thermal conductivity in-plane (ab(xy)-plane) and out of plane (c(z)-axis) are represented by hollow markers and solid markers, respectively, and are compared to available data of experiment [10,12, 15,17,33,34] and density functional theory (DFT) calculations [17–20, 35]. The data were directly extracted from thermal conductivity versus temperature graphs in the referenced studies without any modifications.

The κ_L decreases with increasing temperature in both directions for all results in Fig. 5. Temperature dependency of the lattice thermal conductivity of single crystals Mg_3Sb_2 attained in this work, which is based on NEMD simulations combined with two region LT method, is in reasonable agreement with previously suggested experimental and DFT data. Scattered thermal conductivity data of single crystals Mg_3Sb_2 in the present NEMD results mainly arises from the variation of crystallite size, which is unconstraint in all directions. The observed discrepancies between the present calculations and experimental data primarily stem from the following reasons. First, our calculations do not account for grain boundary scattering, as they were performed for a single crystallite. Additionally, the Langevin thermostatting method used in this study does not directly introduce phonon scattering; instead, it influences the

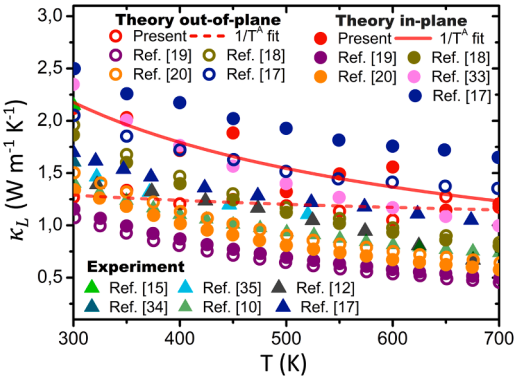


Fig. 5. Temperature dependence of lattice thermal conductivity of single crystalline Mg_3Sb_2. Red solid and dashed lines denote the best fitting to present NEMD results.

system indirectly through the interatomic potential in the central region between the hot and cold thermostats. In contrast to the previous DFT calculations [18,20], our NEMD calculations and earlier DFT calculations [17,19] demonstrate that κ_L in-plane is larger than that of out-of-plane. The anisotropy ratio is estimated as between $\kappa_a/\kappa_c \approx 1.67 - 1.00$ which decreases with increasing temperature from 300 K to 700 K. Although it was suggested that the lattice thermal conductivity of Mg_3Sb_2 is nearly isotropic with the ratio about 1.05–1.10 [18–20], later it was shown that there exists significant anisotropy of $\kappa_a/\kappa_c \approx 1.22$ [17] and $\kappa_a/\kappa_c \approx 1.44$ [21], and also reduces with increasing temperature between 300K-700 K [17] but not as much as in present NEMD results. The anisotropy of thermal conductivity arises directly from directional variations in interatomic bond strength. Strong covalent bonds enhance phonon group velocities and thermal conductivity along specific crystallographic axes, whereas weaker ionic or van der Waals interactions reduce these properties in directions dominated by such bonding. The enhanced anisotropy observed in single-crystalline layered structure of Mg_3Sb_2 compared to polycrystalline counterparts has been attributed to disparities in average group velocities between in-plane and out-of-plane directions, as well as distinct chemical bonding characteristics within layers (intralayer) versus between layers (interlayer) [17,21]. As temperature increases, atoms gain energy, and phonons vibrate more frequently. This intensifies Umklapp scattering processes, which reduce the average distance phonons travel before scattering (i.e., the mean free path). Concurrently, lattice expansion weakens interatomic bonds. These mechanisms explain the decrease in lattice thermal conductivity with rising temperature, consistent with prior studies (Fig. 5) [19,21]. In Mg_3Sb_2, weak chemical bonding and anharmonic potential wells indicate strong anharmonic scattering, key factors contributing to its low thermal conductivity. The layered structure further accentuates anisotropic thermal transport: out-of-plane directions exhibit weaker interatomic bonds (e.g., van der Waals interactions), resulting in shorter phonon mean free paths and slower group velocities compared to in-plane directions [17,21]. Consequently, heat flow is hindered out-of-plane, leading to the observed thermal conductivity anisotropy.

Although the lattice thermal conductivity of crystalline materials is, generally, inversely proportional to temperature (T^{-1}) at high temperatures, theoretical and experimental studies have reported that the thermal conductivity of Mg_3Sb_2 exhibits a weaker temperature dependent behaviour of $T^{-0.48} \sim T^{-0.90}$ [17]. The relation between the κ_L and temperature in our NEMD simulation is obtained by fitting a function of the form T^{-A}, solid red curve (in-plane) and dashed red curve (out-of--plane) in Fig. 5. The obtained temperature dependence of κ_L of single crystalline Mg_3Sb_2 along in-plane and out-of-plane directions can be characterised by the functions that $T^{-0.67}$ and $T^{-0.14}$, respectively. Present NEMD calculations also demonstrates a weaker temperature dependence of κ_L along in-plane direction with $T^{-0.67}$ which is qualitatively in fairly good agreement with previous experimental and theoretical results of $T^{-0.48} \sim T^{-0.90}$. Despite that κ_L along out-of-plane direction follows a much weaker temperature dependence it is still within the range of data from previous studies at all temperatures.

The difference between the κ_Ls of in-plane and out-of-plane directions is reduced at high temperatures. It is also important to note that, present NEMD results reveal different trends between the temperature dependence of κ_L along the in-plane and out-of-plane directions while it is previously reported that they follow almost the same guideline [17]. Like most layered ionic crystals, Mg_3Sb_2's thermal conductivity anisotropy is expected to diminish at elevated temperatures. This occurs because out-of-plane thermal conductivity is already suppressed by weak bonding, leaving little room for further reduction. In contrast, in-plane thermal conductivity—initially high at low temperatures—declines more rapidly with heating due to stronger Umklapp scattering. This also explains why the temperature dependence of thermal conductivity is much weaker in the out-of-plane direction than in-plane, as observed here.

4. Conclusions

In summary, we have investigated the lattice thermal conductivity κ_L of single crystallite magnesium antimonide (Mg_3Sb_2) between the temperature range of 300 K and 700 K using the nonequilibrium molecular dynamics (NAMD) heat transport simulations technique combined with two region Langevin thermostatting method which mimics real experiment. Interionic interactions were modelled by Buckingham type of rigid ion potential optimised earlier.

We found that the calculated κ_L is significantly low, below ~ 2.0 W $m^{-1}K^{-1}$, and exhibits strong anisotropy at low and mid temperatures and becomes nearly isotropic at high temperatures. Along the in-plane direction κ_L was considerably reduced with increasing temperature that is $\sim 52\%$ from 300 K and 700 K, while that of along the out-of-plane direction exhibited very slow reduction of $\sim 18\%$ only. Moreover, the κ_L deviates from the typical T^{-1} law and demonstrates an anomalously weaker temperature dependence in the in-plane direction described as $T^{-0.67}$, as in previously published experimental and DFT results. But unexpectedly, it is much weaker and follows different trend along the out-of-plane direction with $T^{-0.14}$. These are important to enhance the figure of merit of Mg_3Sb_2 as a potential material in thermoelectric applications. Overall, we presented that NEMD simulation with two region thermostatting methodology successfully demonstrates the heat transport in single crystalline Mg_3Sb_2.

The combination of anisotropic and low thermal conductivity in layered single crystals allows precise control over heat flow, making them essential for energy conversion, electronics, and thermal management systems. It has been shown that the thermal conductivity can be enhanced and manipulated from anisotropic to isotropic via mechanical strain and external electric field applications. This enables real-time tuning of thermal properties in adjustable thermoelectric devices, a step toward adaptive thermal systems [36–38]. We believe that current work conducted here to investigate the lattice thermal conductivity of single crystalline Mg_3Sb_2 will encourage future studies on Mg_3Sb_2 based zintl materials which is necessary for the development of thermoelectric devices.

CRediT authorship contribution statement

Günay Seçkin D.: Methodology, Investigation. **Akdere Ünsal:** Visualization, Software. **Taşseven Çetin:** Writing – original draft.

Declaration of Competing Interest

The authors declare that they have no known competing financial interests or personal relationships that could have appeared to influence the work reported in this paper.

Acknowledgments

ÇT gratefully acknowledges the sabbatical support between September 2023 and August 2024 by the Yıldız Technical University and the hosting by the University of East Anglia.

Data availability

Data will be made available on request.

References

[1] Q. Zheng, M. Hao, R. Miao, J. Schaadt, C. Dames, Advances in thermal conductivity for energy applications: a review, Prog. Energy 3 (2021) 012002, https://doi.org/10.1088/2516-1083/abd082.

[2] A.L. Moore, L. Shi, Emerging challenges and materials for thermal management of electronics, Mater. Today 17 (4) (2014) 163–174, https://doi.org/10.1016/j.mattod.2014.04.003.
[3] W. Xing, Y. Xu, C. Song, T. Deng, Recent advances in thermal interface materials for thermal management of high-power electronics, Nanomaterials 12 (19) (2022), https://doi.org/10.3390/nano12193365.
[4] Y. Jung, M. Kim, T. Kim, J. Ahn, J. Lee, S.H. Ko, Functional materials and innovative strategies for wearable thermal management applications, Nano-Micro Lett. 15 (2023) 160, https://doi.org/10.1007/s40820-023-01126-1.
[5] P.A. Finn, C. Asker, K. Wan, E. Bilotti, O. Fenwick, C.B. Nielsen, Thermoelectric materials: current status and future challenges, Front. Electron. Mater. 1 (2021) 677845, https://doi.org/10.3389/femat.2021.677845.
[6] C. Gayner, K.K. Kar, Recent advances in thermoelectric materials, Prog. Mater. Sci. 83 (2016) 330–382, https://doi.org/10.1016/j.pmatsci.2016.07.002.
[7] S.M. Kauzlarich, K.P. Devlin, C.J. Perez, 2.5 - Zintl phases for thermoelectric applications, in: R. Funahashi (Ed.), Thermoelectric Energy Conversion, Woodhead Publ., 2021, pp. 157–182, https://doi.org/10.1016/B978-0-12-818535-3.00004-9.
[8] G. Han, Y. Lu, H. Jia, Z. Ding, L. Wu, Y. Shi, G. Wang, O. Luo, Y. Chen, J. Wang, G. Huang, X. Zhou, Q. Li, F. Pan, Magnesium-based energy materials: progress, challenges, and perspectives, J. Magnes. Alloy 11 (11) (2023) 3896–3925, https://doi.org/10.1016/j.jma.2023.08.009.
[9] Z. Zhou, G. Han, X. Lu, G. Wang, X. Zhou, High-performance magnesium-based thermoelectric materials: progress and challenges, J. Magnes. Alloy 10 (7) (2022) 1719–1736, https://doi.org/10.1016/j.jma.2022.05.021.
[10] L. Song, J. Zhang, B.B. Iversen, Simultaneous improvement of power factor and thermal conductivity via Ag doping in p-type Mg3Sb2 thermoelectric materials, J. Mater. Chem. A 5 (10) (2017) 4932–4939, https://doi.org/10.1039/C6TA08316A.
[11] J. Shuai, Y. Wang, H.S. Kim, Z. Liu, J. Sun, S. Chen, J. Sui, Z. Ren, Thermoelectric properties of Na-doped Zintl compound: Mg3−xNaxSb2, Acta Mater. 93 (2015) 187–193, https://doi.org/10.1016/j.actamat.2015.04.023.
[12] A. Bhardwaj, D.K. Misra, Enhancing thermoelectric properties of a p-type Mg3Sb2-based Zintl phase compound by Pb substitution in the anionic framework, RSC Adv. 4 (65) (2014) 34552–34560, https://doi.org/10.1039/C4RA04889J.
[13] J. Zhang, L. Song, B.B. Iversen, Insights into the design of thermoelectric Mg3Sb2 and its analogs by combining theory and experiment, NPJ Comput. Mater. 5 (2019) 76, https://doi.org/10.1038/s41524-019-0215-y.
[14] X. Ma, K. Liu, F. Cao, Q. Zhang, J. Mao, Single-crystalline Mg3Sb2-xBix-based thermoelectric materials, Cell Rep. Phys. Sci. 5 (3) (2024) 101875, https://doi.org/10.1016/j.xcrp.2024.101875.
[15] J. Xin, G. Li, G. Auffermann, H. Borrmann, W. Schnelle, J. Gooth, X. Zhao, T. Zhu, C. Felser, C. Fu, Growth and transport properties of Mg3X2 (X = Sb, Bi) single crystals, Mater. Today Phys. 7 (1) (2018) 61–68, https://doi.org/10.1016/j.mtphys.2018.11.004.
[16] Y. Pan, M. Yao, X. Hong, Y. Zhu, F. Fan, K. Imasato, Y. He, C. Hess, J. Fink, J. Yang, B. Büchner, C. Fu, G.J. Snyder, C. Felser, Mg3(Bi,Sb)2 single crystals towards high thermoelectric performance, Energy Environ. Sci. 13 (6) (2020) 1717–1724, https://doi.org/10.1039/D0EE00838A.
[17] Y. Zhu, Y. Xia, Y. Wang, Y. Sheng, J. Yang, C. Fu, A. Li, T. Zhu, J. Luo, C. Wolverton, G.J. Snyder, J. Liu, W. Zhang, Violation of the T^{-1} relationship in the lattice thermal conductivity of Mg3Sb2 with locally asymmetric vibrations, AAAS Res. 2020 (2020) 4589786, https://doi.org/10.34133/2020/4589786.
[18] F. Meng, S. Sun, J. Ma, C. Chronister, J. He, W. Li, Anisotropic thermoelectric figure-of-merit in Mg3Sb2, Mater. Today Phys. 13 (2020) 100217, https://doi.org/10.1016/j.mtphys.2020.100217.
[19] J. Zhang, L. Song, M. Sist, K. Tolborg, B.B. Iversen, Chemical bonding origin of the unexpected isotropic physical properties in thermoelectric Mg3Sb2 and related materials, Nat. Commun. 9 (2018) 4716, https://doi.org/10.1038/s41467-018-06980-x.
[20] S. Huang, Z. Wang, R. Xiong, H. Yu, J. Shi, Significant enhancement in thermoelectric performance of Mg3Sb2 from bulk to two-dimensional monolayer, Nano Energy 62 (2019) 212–219, https://doi.org/10.1016/j.nanoen.2019.05.028.
[21] A. Li, C. Hu, B. He, M. Yao, C. Fu, Y. Wang, X. Zhao, C. Felser, T. Zhu, Demonstration of valley anisotropy utilized to enhance the thermoelectric power factor, Nat. Commun. 12 (2021) 5408, https://doi.org/10.1038/s41467-021-25722-0.
[22] A. Jain, S.P. Ong, G. Hautier, W. Chen, W.D. Richards, S. Dacek, S. Cholia, D. Gunter, D. Skinner, G. Ceder, K.A. Persson, Commentary: the materials project: a materials genome approach to accelerating materials innovation, APL Mater. 1 (2013) 011002, https://doi.org/10.1063/1.4812323.
[23] C. Zheng, R. Hoffmann, R. Nesper, H.G. von Schnering, Site preferences and bond length differences in $CaAl_2Si_2$-type Zintl compounds, J. Am. Chem. Soc. 108 (8) (1986) 1876–1884, https://doi.org/10.1021/ja00268a027.
[24] M. Martinez-Ripoll, A. Haase, G. Brauer, The crystal structure of α-Mg_3Sb_2, Acta Crystallogr. Sect. B Struct. Crystallogr. Cryst. Chem. 30 (8) (1974) 2006–2009, https://doi.org/10.1107/S0567740874006285.
[25] Ü. Akdere, S.D. Günay, Ç . Taşseven, Ordering and diffusion in liquid magnesium antimonide (Mg3Sb2) from hypernetted-chain theory and molecular dynamics simulation, Ionics 25 (2019) 2711–2717, https://doi.org/10.1007/s11581-018-2757-2.
[26] M.S. Green, Markoff random processes and the statistical mechanics of time-dependent phenomena. II. Irreversible processes in fluids, J. Chem. Phys. 22 (3) (1954) 398–413, https://doi.org/10.1063/1.1740082.
[27] R. Kubo, Statistical–mechanical theory of irreversible processes. I. General theory and simple applications to magnetic and conduction problems, J. Phys. Soc. Jpn. 12 (6) (1957) 570–586, https://doi.org/10.1143/JPSJ.12.570.
[28] W.G. Hoover, C.G. Hoover, Nonequilibrium molecular dynamics, Condens. Matter Phys. 8 (2(42) (2005) 247–260, https://doi.org/10.5488/CMP.8.2.247.
[29] T. Ikeshoji, Hafskjold, Non-equilibrium molecular dynamics calculation of heat conduction in liquid and through liquid-gas interface, Mol. Phys. 81 (2) (1994) 251–261, https://doi.org/10.1080/00268979400100171.
[30] P. Wirnsberger, D. Frenkel, C. Dellago, An enhanced version of the heat exchange algorithm with excellent energy conservation properties, J. Chem. Phys. 143 (2015) 124104, https://doi.org/10.1063/1.4931597.
[31] A.P. Thompson, H.M. Aktulga, R. Berger, D.S. Bolintineanu, W.M. Brown, P. S. Crozier, P.J. in 't Veld, A. Kohlmeyer, S.G. Moore, T.D. Nguyen, R. Shan, M. J. Stevens, J. Tranchida, C. Trott, S.J. Plimpton, LAMMPS - a flexible simulation tool for particle-based materials modeling at the atomic, meso, and continuum scales, Comput. Phys. Commun. 271 (2022) 108171, https://doi.org/10.1016/j.cpc.2021.108171.
[32] F. Müller-Plathe, A simple nonequilibrium molecular dynamics method for calculating the thermal conductivity, J. Chem. Phys. 106 (1997) 6082, https://doi.org/10.1063/1.473271.
[33] S.H. Kim, C.M. Kim, Y.K. Hong, K.I. Sim, J.H. Kim, T. Onimaru, T. Takabatake, M. H. Jung, Thermoelectric properties of Mg3Sb2−xBix single crystals grown by Bridgman method, Mater. Res. Express 2 (5) (2015) 055903, https://doi.org/10.1088/2053-1591/2/5/055903.
[34] S. Kim, C. Kim, Y.K. Hong, T. Onimaru, K. Suekuni, T. Takabatake, M.H. Jung, Thermoelectric properties of Mn-doped Mg–Sb single crystals, J. Mater. Chem. A. 2 (2014) 12311, https://doi.org/10.1039/C4TA02386B.
[35] J. Ding, T. Lanigan-Atkins, M. Calderón-Cueva, A. Banerjee, D.L. Abernathy, A. Said, A. Zevalkink, O. Delaire, Soft anharmonic phonons and ultralow thermal conductivity in $Mg_3(Sb,Bi)_2$ thermoelectrics, Sci. Adv. 7 (21) (2021) eabg1449, https://doi.org/10.1126/sciadv.abg1449.
[36] Z. Yang, K. Yuan, J. Meng, M. Hu, Electric field tuned anisotropic to isotropic thermal transport transition in monolayer borophene without altering its atomic structure, Nanoscale 12 (2020) 19178–19190, https://doi.org/10.1039/D0NR03273E.
[37] N.S. Ha, T.M. Pham, H. Hao, G. Lu, Energy absorption characteristics of bio-inspired hierarchical multi-cell square tubes under axial crushing, Int. J. Mech. Sci. 201 (2021) 106464, https://doi.org/10.1016/j.ijmecsci.2021.106464.
[38] X.K. Cheg, E.M. Zhang, D. Wu, K.Q. Cheg, Strain-induced medium-temperature thermoelectric performance of Cu_4TiSe_4: the role of four-phonon scattering, Phys. Rev. Appl. 19 (2023) 044052, https://doi.org/10.1103/PhysRevApplied.19.044052.